

## The effects of laser-sheet misalignment on Stereo-PIV measurements in wall-bounded turbulence

G. V. Rama Reddy, J. Philip and I. Marusic

Department of Mechanical Engineering  
 University of Melbourne, Victoria 3010, Australia

### Abstract

The present study attempts to quantify the effects of misalignment of a laser sheet with a calibration target in Stereoscopic-PIV (SPIV) on the measured flow-statistics in wall-bounded turbulence. For this purpose, numerical investigations and SPIV experiments are performed in a fully-developed, turbulent channel flow. The simulations are performed using synthetic particle images generated from Direct Numerical Simulations data of a channel flow [3] in the streamwise  $\times$  wall-normal plane at friction-Reynolds number equal to 934. Angular misalignments ( $\theta$ ) are imposed about the wall-normal axis and translational misalignments ( $\Delta y$ ) along the spanwise direction. The results indicate that for  $\theta = 1^\circ$  and  $\Delta y =$  half the thickness of the laser-sheet ( $L_s$ ), which are the typical maximum misalignments that might be encountered, the errors in the root-mean-square (r.m.s.) velocities in all the three directions are less than 4%. This conclusion agrees well with the experimental data for the negligibly misaligned case. The simulations on larger misalignments (for  $\theta = 5^\circ$  and  $\Delta y = L_s$ ), however, reveal a significant effect for the wall-normal r.m.s. velocity.

### Introduction

There are many experimental parameters in Stereoscopic-PIV (SPIV) that dictate the accuracy of the final reconstructed velocity field and hence the statistics. Stereo-angle between the cameras, alignment between the laser sheet and the calibration surface, intensity profile across the laser sheet, background noise in the images and laser sheet thickness, are a few examples. In the studies on SPIV (Coudert and Schon [1]; Giordano and Astarita [4]; Lawson and Lawson [7]; Scarano *et al* [10]; Wieneke [12] amongst others), the stereo-angle is fixed while investigating the effects of the other parameters. Regarding the laser sheet misalignment, recent studies have developed tools to assess and account for the misalignments. Coudert and Schon [1] proposed an algorithm for correcting the misalignments, which was tested using synthetic random patterns and experiments in turbulent water jets. Scarano *et al* [10] compared calibration accuracies of two techniques for different linear misalignments using synthetic particle patterns. Significant improvement was achieved by Wieneke [12], who developed a self-calibration technique as a means to correct a larger range of misalignments. In their scanning-SPIV set-up, Lawson and Dawson [7] tested Wieneke's self-calibration method on isotropic turbulence by systematically applying perturbations (misalignments) to their camera set-up, in addition to investigating other parameters.

To date, there has been no systematic study to quantify the effects of laser sheet misalignments and the choice of a stereo-angle on the turbulence statistics in wall-bounded turbulence. This is because most parametric studies are performed on random patterns. As such, the present study investigates the misalignment effects on wall-bounded turbulence by conducting numerical investigations based on a pre-existing Direct Numerical Simulations (DNS) database and SPIV experiments in fully-developed, turbulent channel flows. The following sections discuss a synthetic particle image generation technique

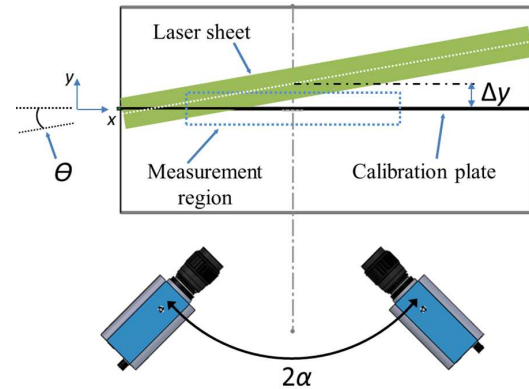


Figure 1: Plan-view-schematic of an SPIV system in which the laser sheet is displaced from the calibration plane due to the imposed angular ( $\theta$ ) and translational ( $\Delta y$ )-misalignments. Here  $2\alpha$  is the stereo-angle between the cameras.

and the methods employed to quantify the misalignments. In the present study,  $x$ ,  $y$ ,  $z$  denote the streamwise, the spanwise and the wall-normal directions, respectively, with  $u'$ ,  $v'$  and  $w'$  indicate the corresponding turbulence r.m.s. velocity components.

### Simulations

#### Generation of synthetic particle images

Figure (1) shows a plan-view-schematic of the SPIV configuration, where the laser sheet experiences both angular ( $\theta$ ) and translational ( $\Delta y$ ) misalignments. In the present study, however, only one misalignment parameter is varied at a time. Using the in-house PIV package developed at the University of Melbourne (De Silva *et al* [2]), synthetic images are generated from the DNS of velocity fields of Del Alamo *et al* [3] (at friction-Reynolds number,  $Re_\tau = 934$ ) in the perfectly orthogonal  $xz$ -plane. Here  $\theta$  and  $\Delta y$  are imposed by misaligning the stereo-angle. In the present study, we utilize all three velocity components taken from 90 simulation volumes, which are found to be sufficient for achieving the convergence of r.m.s. velocity components. The dimensions of each volume in wall-units are  $1238 \times 26 \times 1074$  in the  $x$ ,  $y$  and the  $z$  directions, respectively.

In the present investigation, we impose  $\theta$  equal to  $0^\circ$ ,  $1^\circ$  and  $5^\circ$  and  $\Delta y$  equal to  $L_s/2$  and  $L_s$ , where  $L_s$  is the thickness of the laser sheet, which is 1.5 mm, if half-channel height in the DNS-data is considered to be 50 mm. Here  $\theta = 0^\circ$  (with  $\Delta y = 0$  mm) corresponds to the perfectly aligned case. We fix the stereo-angle  $2\alpha$  (see figure (1)) to be  $75^\circ$ . At this angle, we found that the turbulence statistics have least discrepancies with the DNS. The virtual camera sensor size is  $1730 \text{ pixel} \times 1730 \text{ pixel}$ . For all the cases considered, the total number of particles in the volume of the DNS data imaged is maintained to be  $2 \times 10^5$ . The Phong lighting model is used to simulate the illu-

mination of synthetic particles (spheres) by the laser sheet and no background noise is simulated. The resulting particle size in the images is 2 to 3 pixel units approximately. Further, no lens aberrations are modelled while generating the particle images.

### Calibration and reconstruction methods

In the present study, the self-calibration (correction) of Wieneke [12], together with the three-component velocity reconstruction method of Willert [13] is considered, and is referred to as method-A. Method-A serves as a base for method-B, which is that of Soloff *et al* [11]. In both the methods, images of circular dots in five parallel planes are used for calibration, where the extreme planes are separated by the distance equal to  $L_s$ . Further, a standard PIV algorithm using the hierarchical interrogation method (Willert [13]) and iterative window-deformation (Jambunathan *et al* [6]; Scarano [9]) schemes is used for computing two-component (2C) velocity field from pairs of particle images of each camera.

In method-A, self-calibration of Wieneke [12] is employed for camera-calibration and correction of misalignments. In the simulations, the recorded views are calibrated using the standard linear camera-pinhole-model (Hartley and Zisserman [5]), as the synthetic particles are generated without any camera-lens-model. For the experimental image processing, however, a radial-distortion model of 2<sup>nd</sup> order is used. The self-calibration algorithm predicts and corrects for the misalignments iteratively. Since it involves decomposition of the projection matrix into matrices of intrinsic and extrinsic camera parameters, we are able to obtain the positions of the cameras with respect to the object space, and hence the viewing-angles for all the particle displacements. The camera-positions could be used to validate the stereo-angles chosen while generating the synthetic images. Further, knowing the exact viewing-angles allows us to use the simple geometric relations proposed by Willert [13] to reconstruct the three-component velocity field. Self-calibration algorithm will also predict angular misalignments about the  $x$ -axis ( $\phi$ ). However, it is fixed to be  $0^\circ$  for all the simulations.

Method-B calibrates cameras through 3<sup>rd</sup> order polynomial mapping equations [11]. The mapping functions express pixel coordinates (in the image plane) in terms of physical units (in the real space). Derivatives of the mapping functions are then used to calculate three components of the velocity field in the real space from the 2C velocity field of the two cameras using a least-squares error method. The final interrogation window (IW) size for both self-calibration and computation of the velocity field is chosen to be 32 pixel  $\times$  32 pixel, with 50% overlap of successive windows. The resulting spatial resolution of the velocity field is 20 wall-units approximately. The DNS velocity fields are volume-averaged to match this spatial resolution in the simulations for enabling comparison of the flow-statistics. Spurious vectors, if any found, are detected using a standard median filter, and bicubic interpolation is used for vector replacements.

## Results and Discussion

### Performance of self-calibration of method-A:

Before assessing the methods for the range of misalignments imposed in the simulations, the self-calibration of method-A is tested for the perfectly-aligned case. The stereo-angles are predicted to the accuracy of 0.3%. The residual misalignments obtained after correction are presented in table 1. The values indicate that the self-calibration performs well within the tolerable accuracy.

Parameter	Residuals after applying method-A		
	$\theta$	$\phi$	$\Delta y^+$
<b>Simulations: Angular</b> ( $\phi = 0^\circ$ & $\Delta y^+/l^+ = 0$ )			
$\theta = 0^\circ$ (Aligned case)	0.014 $^\circ$	0.013 $^\circ$	0.39
$\theta = 1^\circ$	0.0034 $^\circ$	0.0098 $^\circ$	0.46
$\theta = 5^\circ$	0.0025 $^\circ$	0.024 $^\circ$	0.38
<b>Simulations: Translational</b> ( $\theta = 0^\circ$ & $\phi = 0^\circ$ )			
$\Delta y^+/l^+ = 0.62$	0.025 $^\circ$	0.018 $^\circ$	0.74
$\Delta y^+/l^+ = 1.24$	0.021 $^\circ$	0.038 $^\circ$	2.00
<b>Experiments</b>			
$\theta = 0^\circ$ ; $\phi = 0^\circ$ & $\Delta y^+/l^+ = 0$	0.0074 $^\circ$	0.016 $^\circ$	0.36

Table 1: List of the residual misalignments obtained by the self-calibration algorithm in method-A, after correcting for the imposed misalignments in the simulations and that predicted in the experiments.

### Assessment on angular misalignments:

Since method-A employs the self-calibration, the velocities predicted are expected to be close to that of the perfectly-aligned case, irrespective of the misalignment-type and degree. However, it is found even in method-B of our simulations (as well as in the experiments discussed later in the article) that the mean velocity ( $U$ ) and the normalized r.m.s. velocity ( $u'^+ = u'/u_\tau$ ) in the streamwise direction are of the same order as that of the aligned case. Here  $u_\tau$  is the friction velocity. Further, the magnitudes are of same order as that of method-A. This implies that  $U$  and  $u^+$  are insensitive to these misalignments, and it could be due to their spanwise homogeneity.  $U$  and  $u'^+$  would become sensitive, if the  $xy$ -plane was chosen, as  $U$  varies significantly along  $z$ , and any rotational misalignment about the  $y$ -axis would cause considerable departures from the DNS predictions. In the present study, we show the distributions of the r.m.s. velocities in the wall-normal and the spanwise directions, which show little or more deviations with the filtered DNS curves for the imposed misalignments, and do not present that of  $U$  and  $u'^+$ .

Figures (2) and (3) show the normalized turbulence r.m.s. velocities in the spanwise ( $v'^+ = v'/u_\tau$ ) and the wall-normal ( $w'^+ = w'/u_\tau$ ) directions, along with the corresponding curves of the unfiltered (solid black line) and the filtered (solid red line) DNS. The figures show that, as expected, all the curves of method-A collapse for both  $v'^+$  and  $w'^+$ . However in method-B, when compared with  $v'^+$ , the effects of angular misalignments are pronounced for  $w'^+$  at larger  $\theta$  ( $= 5^\circ$ ). This is more evident from figures 4(a) and 4(b), which show the absolute percentage deviations of  $v'^+$  and  $w'^+$  from the filtered-DNS data in the logarithmic region. In method-B, the discrepancies of  $v'^+$  are approximately of same order for all  $\theta$ . However,  $w'^+$  involves comparable discrepancies only when  $\theta > 1^\circ$ , and it is as high as 7% at  $\theta = 5^\circ$ . It seems that the error incurred due to the imposed angular misalignments is very small to influence  $v'^+$ , but it affects  $w'^+$  at very large  $\theta$ . In light of these, it seems that we obtain reasonable flow-statistics even when misalignments of order  $\theta \leq 1^\circ$  are not corrected for. However, a further investigation is required to find out whether slightly higher (but  $< 5^\circ$ ) angular misalignments are also tolerable. Since it is easy to notice such tolerable misalignments while positioning the laser sheet, measurements may be proceeded without adversely affecting the flow-statistics. It can also be noticed that the devia-

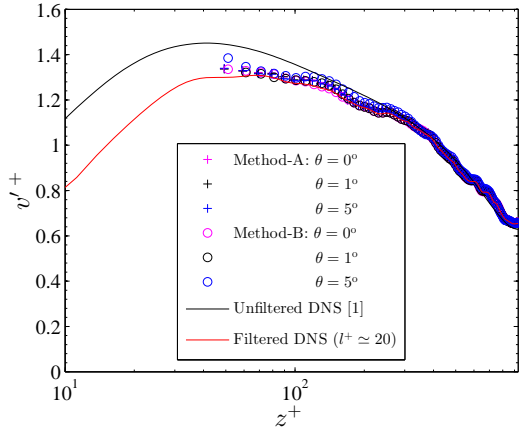


Figure 2: Comparison of the normalized r.m.s. velocities in the spanwise direction ( $v'^+$ ) with that of the filtered-DNS data for the angular misalignments discussed in the study.

tions in method-B are slightly smaller than that of method-A for  $\theta \leq 1^\circ$ . Hence, together with the attracting aspect of ease in the implementation, it prompts one to prefer method-B when such smaller misalignments are encountered during the alignment.

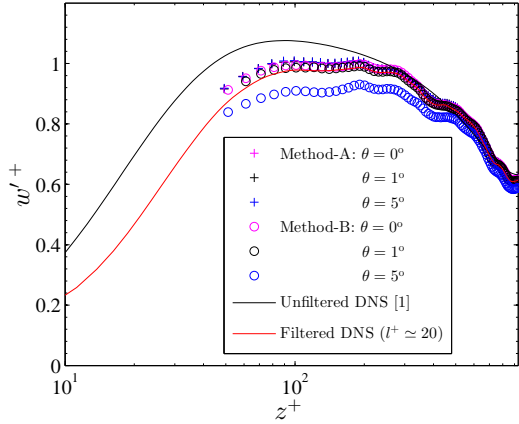


Figure 3: Comparison of the normalized r.m.s. velocities in the wall-normal direction ( $w'^+$ ) with that of the filtered-DNS data for the angular misalignments discussed in the study.

#### Assessment on translational misalignments

Figure (5) shows the normalized r.m.s. velocities in the spanwise direction along with the curves of the filtered and the unfiltered DNS. The distributions of  $v'^+$  of method-B are comparable to that of method-A for all the translational misalignments. This can also be noticed from figure 6(a), which shows the absolute percentage deviations of  $v'^+$  from that of the filtered DNS. It could be that the errors caused by these misalignments are too small to influence  $v'^+$ . However,  $w'^+$  gets affected with the presence of larger translational misalignments, as can be inferred from figure (7). When  $\Delta y = L_s/2$  (or  $\Delta y^+/l^+ = 0.62$ ), there is hardly any difference between the results produced by both method-A and B and the filtered DNS. Here  $l^+ \approx 20$  is the size of the IW in wall-units. This is more obvious from figure 6(b), which shows the absolute percentage deviations of  $w'^+$  in the logarithmic region. However, when  $\Delta y = L_s$  i.e. when the laser sheet is completely outside the calibration region (or  $\Delta y^+/l^+ = 1.24$ ),  $w'^+$  of method-B involves larger discrepancies compared to the other cases. It implies that the effect of the translational misalignment is dominant at such larger  $\Delta y$ . In summary, when  $\Delta y^+/l^+ = 0.62$ , the errors in the r.m.s. velocities are tolerable, even if such misalignments are left un-

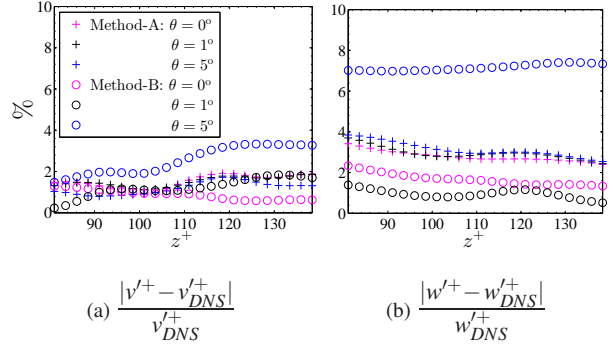


Figure 4: Absolute percentage deviations of the normalized r.m.s. velocities along (a) the spanwise and (b) the wall-normal directions for different angular misalignments. The deviations are obtained from the filtered DNS data in the logarithmic region. The legend in (b) is same as that of (a).

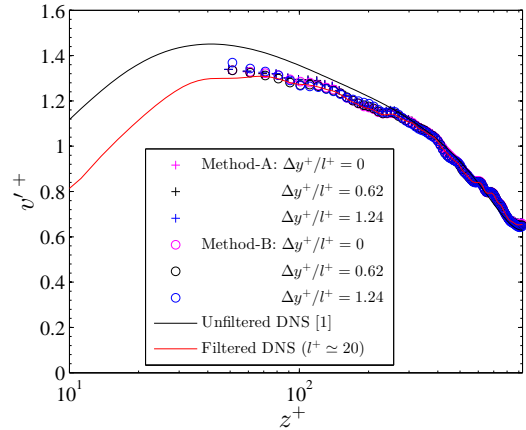


Figure 5: Comparison of the normalized r.m.s. velocities in the spanwise direction ( $v'^+$ ) with that of the filtered-DNS data for the translational-misalignments discussed in the study.

corrected. Further, as observed for smaller angular misalignments, the accuracy of method-B is slightly better than that of method-A for smaller  $\Delta y$ . Since these tolerable misalignments are not difficult to visualize during the alignment, one may proceed with the measurements and prefer method-B, as it is relatively simple to implement, too. However, if method-A is ready to use, it is always beneficial to use method-A over B.

#### Experiments:

In order to verify the results of the simulations, SPIV experiments were conducted in a fully-developed turbulent flow at  $Re_\tau \approx 934$ , in a channel flow facility available in the University of Melbourne [8]. In these experiments, the laser sheet and the calibration plane are aligned. Two CCD cameras (PCO 4000) equipped with 180 mm camera lenses are used for imaging a  $xz$ -plane in the flow field of size 135 mm  $\times$  90 mm. The stereo-angle  $2\alpha$  between them is  $75^\circ$ . The spatial resolution (26 pixel/mm) in the  $x$  direction is same for both camera images, while that in the  $y$  direction varies as  $29 \pm 10\%$  pixel/mm. The flow is seeded with polyamide particles with mean diameter of  $1\mu\text{m}$ , and illuminated using 1.5 mm thick laser sheet generated using Nd:YAG laser (Evergreen Inc.) and a series of cylindrical lenses. The experimental data are processed using the aforementioned methods.

It is found that the laser sheet and the calibration plane are almost right on top of each other, as the residuals shown in table 1 (last row) are obtained after the 1<sup>st</sup> iteration. Figures 8(a) and

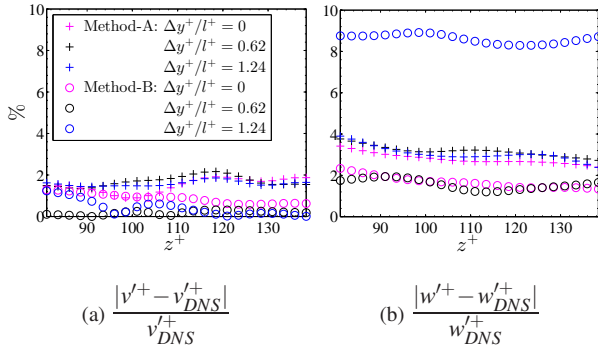


Figure 6: Absolute percentage deviations of the normalized r.m.s. velocities along (a) the spanwise and (b) the wall-normal directions for different translational-misalignments. The deviations are obtained from the filtered DNS data in the logarithmic region. The legend in (b) is same as that of (a).

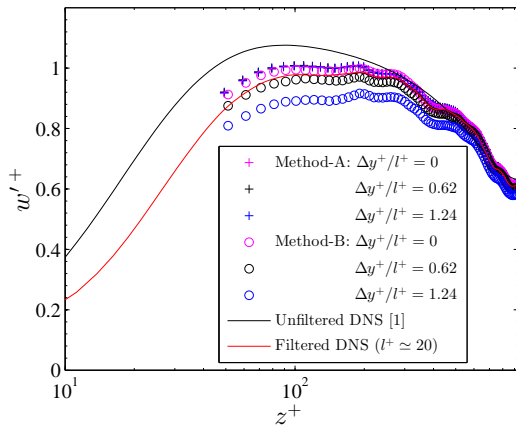


Figure 7: Comparison of the normalized r.m.s. velocities in the wall-normal direction ( $w'^+$ ) with that of the filtered-DNS data for the translational-misalignments discussed in the study.

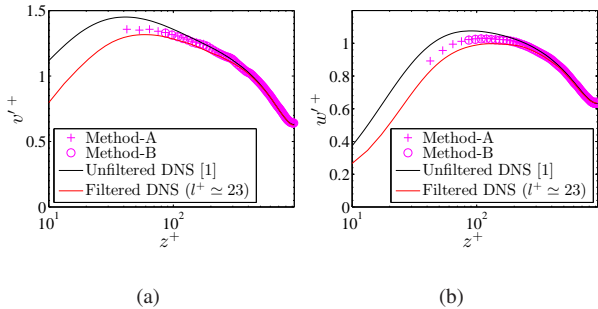


Figure 8: Comparison of the normalized r.m.s. velocities obtained in the experiments with that of the filtered DNS data. (a) Spanwise direction and (b) Wall-normal direction.

8(b) show the curves of  $v'^+$  and  $w'^+$  along with the corresponding curves of the unfiltered DNS and the DNS data filtered to  $t^+ \simeq 23$ . The figures suggest that both the methods perform comparably, even for the real images. This serves as a validation of the performance of the methods used in the simulations for the aligned case.

### Conclusions

Numerical investigations using the DNS database reveal that the misalignments of order  $\theta = 1^\circ$  or  $\Delta y^+/l^+ = 0.62$ , admit acceptable velocity statistics in fully-developed, wall-bounded turbulent flows, even if they are not corrected for. Further,

even at very large misalignments ( $\theta = 5^\circ$  or  $\Delta y^+/l^+ = 1.24$ ), only the r.m.s. velocity in the wall-normal direction is affected and requires calibration-correction. The r.m.s. velocities in the other directions may become sensitive when misalignment occurs along planes, where the flow is statistically inhomogeneous, for instance, an  $xy$ -plane (at a given  $z$ ) with angular misalignments about the  $y$ -axis. Finally, when such tolerable misalignments are observed during the alignment-stage, measurements may be proceeded and method-B (due to Soloff [11]) be preferred, as it is relatively easy to implement and comparably accurate. However, if noticeable bias in the statistics are observed with method-B, one still can resort to self-calibration of method-A.

### Acknowledgements

The authors gratefully acknowledge the financial support of the Australian Research Council, and thank Kevin for providing code for method-B.

### References

- [1] S. Coudert and J. P. Schon. Back-projection algorithm with misalignment corrections for 2d3c Stereoscopic PIV. *Meas. Sci. Technol.*, 12(9):1371, 2001.
- [2] C. M. De Silva, R. Baidya, M. Khashehchi, and I. Marusic. Assessment of Tomographic PIV in wall-bounded turbulence using direct numerical simulation data. *Exp. Fluids*, 52(2):425–440, 2012.
- [3] J. C. Del Alamo, J. Jiménez, P. Zandonade, and R. D. Moser. Scaling of the energy spectra of turbulent channels. *J. Fluid Mech.*, 500:135–144, 2004.
- [4] R. Giordano and T. Astarita. Spatial resolution of the Stereo PIV technique. *Exp. Fluids*, 46(4):643–658, 2009.
- [5] R. Hartley and A. Zisserman. *Multiple view geometry in computer vision*. Cambridge university press, 2003.
- [6] K. Jambunathan, X. Y. Ju, B. N. Dobbins, and S. Ashforth-Frost. An improved cross correlation technique for particle image velocimetry. *Meas. Sci. Technol.*, 6(5):507, 1995.
- [7] J. M. Lawson and J. R. Dawson. A scanning PIV method for fine-scale turbulence measurements. *Exp. Fluids*, 55(12):1–19, 2014.
- [8] J. P. Monty. *Developments in smooth wall turbulent duct flows*. PhD thesis, University of Melbourne, Department of Mechanical and Manufacturing Engineering, 2005.
- [9] F. Scarano. Iterative image deformation methods in PIV. *Meas. Sci. Technol.*, 13(1):R1, 2001.
- [10] F. Scarano, L. David, M. Sbsibi, and D. Calluaud. S-PIV comparative assessment: image dewarping+ misalignment correction and pinhole+ geometric back projection. *Exp. Fluids*, 39(2):257–266, 2005.
- [11] S. M. Soloff, R. J. Adrian, and Z. C. Liu. Distortion compensation for generalized stereoscopic particle image velocimetry. *Meas. Sci. Technol.*, 8(12):1441, 1997.
- [12] B. Wieneke. Stereo-PIV using self-calibration on particle images. *Exp. Fluids*, 39(2):267–280, 2005.
- [13] C. Willert. Stereoscopic digital particle image velocimetry for application in wind tunnel flows. *Meas. Sci. Technol.*, 8(12):1465, 1997.